Efficient Protein Transfection by Swarms of Chemically Powered Plasmonic Virus-Sized Nanorobots

RESSNEROVÁ, A.; NOVOTNÝ, F.; MICHÁLKOVÁ, H.; PUMERA, M.; ADAM, V.; HEGER, Z.

ACS Nano
2021, vol. 15, iss. 8, pp. 12899–12910

ISSN: 1936-0851

DOI: https://doi.org/10.1021/acsnano.1c01172

Accepted manuscript

Efficient Protein Transfection by Swarms of Chemically Powered Plasmonic Virus-Sized Nanorobots

Alzbeta Ressnerova[1,2], Filip Novotny[3], Hana Michalkova[1,2], Martin Pumera[2,3,4,5,6*], Vojtech Adam[1,2†], Zbynek Heger[1,2**]

[1]*Department of Chemistry and Biochemistry, Mendel University in Brno, Zemedelska 1, CZ-613 00 Brno, Czech Republic*

[2]*Central European Institute of Technology, Brno University of Technology, Purkynova 123, CZ-612 00 Brno, Czech Republic*

[3]*Center for the Advanced Functional Nanorobots, Department of Inorganic Chemistry, University of Chemistry and Technology, Technicka 5, CZ-166 28 Prague, Czech Republic*

[4]*Department of Food Technology, Mendel University in Brno, Zemedelska 1, CZ-613 00 Brno, Czech Republic*

[5]*Department of Medical Research, China Medical University Hospital, China Medical University, No. 91 Hsueh-Shih Road, 40402 Taichung, Taiwan*

[6]*Department of Chemical and Biomolecular Engineering, Yonsei University, 50 Yonsei-ro, Seodaemun-gu, 03722 Seoul, Korea*

Corresponding Authors

*Prof. Martin Pumera, Center for the Advanced Functional Nanorobots, University of Chemistry and Technology, E-mail: martin.pumera@vscht.cz

†Prof. Vojtech Adam, Mendel University in Brno, E-mail: vojtech.adam@mendelu.cz

**Dr. Zbynek Heger, Central European Institute of Technology, E-mail: zbynek.heger@ceitec.vutbr.cz

Abstract

Transfection is based on non-viral delivery of nucleic acids or proteins into cells. Viral approaches are being used; nevertheless, their translational capacity is nowadays decreasing due to persistent fear of their safety, therefore creating space for the field of nanotechnology. However, nanomedical approaches introducing static nanoparticles for the delivery of biologically active molecules are very likely to be overshadowed by the vast potential of nanorobotics. We hereby present a rapid non-viral transfection of protein into difficult-to-transfect prostate cancer cell line facilitated by chemically powered rectangular virus-sized (68 × 33 nm) nanorobots. The enhanced diffusion of these biocompatible nanorobots is the key to their fast internalization into cells happening in the matter of minutes being up to 6-fold more efficient compared to static nanorobots in non-fueled environment. Au/Ag plasmonic nature of these nanorobots makes them simply traceable and allows for their detailed subcellular localization. Protein transfection mediated by such nanorobots is an important step forward challenging the field of nanomedicine having the potential in future translational medical research.

Keywords: transfection; nanorobots; metallothionein; protein delivery; protein transfection

Transfection is a research method based on introducing nucleic acids or proteins (or both) into cells using non-viral tools. Stable and robust transfections are not only needed in research to study functions of genes and proteins in cells but also as a first step in development of therapeutical modalities such as protein therapeutics or gene therapy.[1] Delivery of nucleic acids and proteins into cells using viruses has been good for the purposes of basic research but it requires S2 laboratories to work with, and translation from bench to bedside has been complicated due to the safety issues.[2-3] Viruses are feared to be oncogenic and immunogenic, [4-5] and there has been a deviation from their use stably pushing on the area of advanced materials, biomaterials and nanomaterials to develop vehicles with stable transfection performance in basic research while as well, being safe and having further potential in translational research and clinics.

Nanomedicine has been a strong player in this pursuit.[6, 7-10] Gold nanoparticles (Au-NPs) have been extensively used for purposes of transfection of nucleic acids or proteins.[11-12] Au-based nanomaterials are easy to trace due to a surface plasmon resonance, and therefore easy to be visualized.[13] Moreover, Au-NPs exhibit nonimmunogenic and nontoxic properties, making Au a suitable material for translational uses.[14-16] Coupled with high affinity to biomolecules such as proteins, these features are the reason for many applications of Au-NPs in *in Vitro* or *in Vivo* setting. For instance, Au-NPs conjugated with transferrin have been used for imaging and therapy of breast cancer *in Vivo.*[17] Delivering CRISPR-Cas9 gene editing system using nanomaterials has been the shiniest example of delivering both, nucleic acid (gRNA and targeting construct) and protein (Cas9) at once, circumventing the use of viruses, which were usually used for the delivery of gene therapy. Au-NPs loaded with CRISPR-Cas9 gene editing tool have been developed and reported to correct a gene mutation causing Duchenne muscular dystrophy in mice.[18]

Self-propelled autonomous functional micro- and nanorobots ranging in size from the size of a cell to the size of virus have significantly developed in the past decade since their introduction and the whole field witnessed explosive research growth. These functional devices are capable of taking chemical,[19-20] light,[21] or magnetic field energy[22-23] and convert it into the motion.[24] Micro-/nanorobots can have functional surfaces, delivering drugs or performing microsurgeries. Microrobots have been shown to penetrate cell membranes *via* physical force.[25] However, given the size of microrobots, which is comparable to cells, their internalization is not possible. Therefore, sizing down is an essential step in order to use these machines in biological systems.[26]

The latest trend of nanomedicine has been the shift from static to dynamic nanocarriers. The reason for this transition is an insufficient performance of static nanocarriers especially in cancer research characterized by long-term circulation in the bloodstream, low tissue penetration and subsequent poor accumulation in the tumor tissue. [27] Recent studies have shown that nanorobots have the potential to deliver therapeutic molecules more effectively with less off-target accumulation, which points out that autonomous movement of nanocarriers indeed is a key factor.[28-29]

Here, we synthesized biocompatible rectangular virus-sized (68 × 33 nm) nanomachines. These functional nanorobots are composed of silver-coated Au core. Thus, AuAg-nanorobots are plasmonic, which allows their simple tracing within the intracellular space using confocal reflectance microscopy. AuAg-nanorobots exhibit enhanced diffusion in the presence hydrogen peroxide fuel.[30] Here we show that the presence of fuel enhances cellular internalization of AuAg-nanorobots as well. As a proof-of-concept, we proved, that chemically powered AuAg-nanorobots are able to mediate efficient transfection of protein-based [metallothionein (MT)] payload into hard-to-transfect cell line. We show that powered AuAg-nanorobots are swiftly internalizing into cells in matter of minutes, and their

internalization is up to 6-fold more efficient compared to static non-fueled AuAg-nanorobots (**Scheme 1**). The presented system holds a future potential in the field of nanomedicine by upgrading nanocarriers to active nanorobots increasing the efficiency of transport of biologically active molecules.

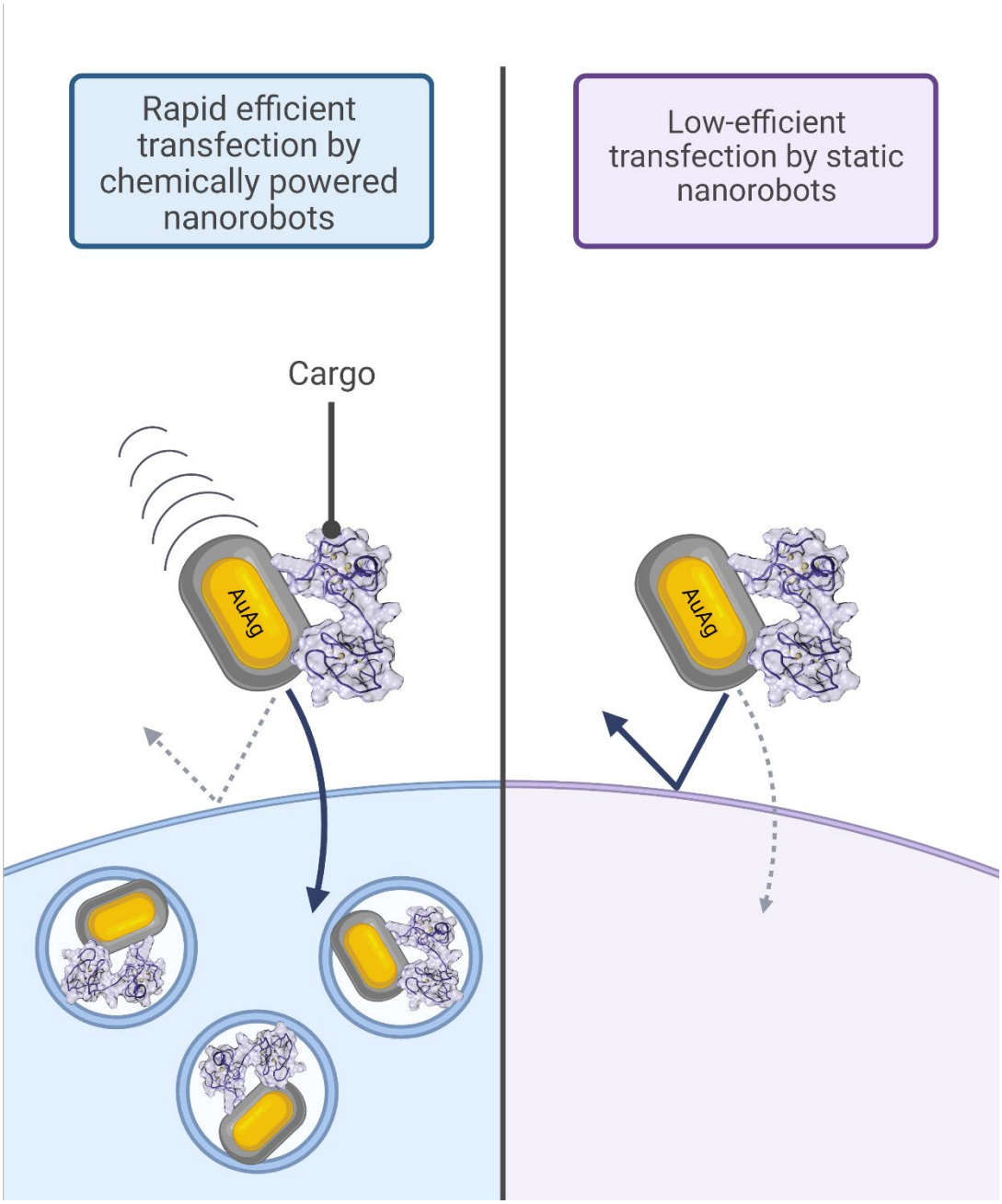

Scheme 1: Internalization of protein cargo (metallothionein, MT) carried by AuAg-nanorobots (gray-gold objects). Transfection by fueled AuAg-nanorobots (left) is markedly

more efficient than transfection by non-fueled AuAg-nanorobots (right). Blue/purple line represents cell membranes, blue circles represent endosomes.

Results/Discussion

Nanorobotics is a field that emerged just recently but that is bringing new challenges and a great potential for a vast number of biomedical applications ranging from diagnostics to therapy.[31] In recent years researches have started to apply nanorobotics in biomedicine aiming to improve transport of biologically active molecules or therapeutics, which is the golden grail of precise therapeutic approach not only in anticancer treatment.[32] That is the response to drawbacks that classical static nanomedicine still battles. Among them, low retention of nanoparticles in target tissues is one of the main issues.[27] Dynamic nanomedicine aims to overcome that with nanorobots capable of autonomous movement. The future are autonomous smart nanorobots capable of guiding themselves directly to the disease site where they carry out their function. This will lead to higher efficiency of transport closely connected with higher efficiency of treatment and less side effects. Moreover, less material will be used, thus nanorobotics could be more economical and environmental-friendly compared to a static nanomedicinal agents.

In the presented study, we utilized nanoscaled virus-size (68 nm long and 33 nm wide) chemically powered AuAg-nanorobots to carry a protein payload (MT) into DU145 cells that represent an androgen-dependent metastatic prostate cancer cell line routinely known for being hard-to-transfect with common molecular biology methodologies. Therefore, the presented study extends the applicability of dynamic nanosystems and underpins their exceptional properties not only for biomedical field.

Synthesis and physico-chemical characterization of AuAg-nanorobots

A three-step wet-chemical method was used to synthesize the rectangular AuAg-nanorobots composed of AuNRs-based core and Ag shell (**Supplementary Fig. 1A**). Such composite

nanoparticles were previously shown to exhibit enhanced diffusion in the presence of hydrogen peroxide.[30] **Supplementary Fig. 1B** shows well-defined monodispersed rectangular AuAg-nanorobots with a mean size of ~68 × 33 nm possessing the size of Au cores of 60.2 ± 8 nm in length and 17 ± 3.4 nm in width with the thickness of Ag shell of 8.4 ± 1.0 nm along the length, and 4.0 ± 0.9 nm at the tips. After the synthesis, the cytotoxic cetyl-trimethyl ammonium chloride (CTAC) stabilizing layer was exchanged for the thiolated analog, 16-mercaptohexadecyl)trimethylammonium bromide (MTAB). MTAB-coated gold AuNRs were shown to possess excellent biogenic properties.[33] The colloidal stability analyses revealed a stable ζ-potential values (38.8 ± 17.2 mV) (**Supplementary Fig. 1C**). EDX elemental mapping confirmed the Au core homogenously covered with catalytic Ag shell (**Supplementary Fig. 1D**). UV-Vis spectrum in **Supplementary Fig. 1E** shows sharp absorption features caused by the coupling of the localized plasmon surface resonance of the plasmonic Au core and Ag shell.[34] The presented synthesis methodology allows for long-term and complex biological experiments, as the AuAg-nanorobots colloid is produced in high-yield (10^{10} p/mL), practical volume, and is long-term stable.[30]

AuAg-nanorobots as biocompatible nanotools

Metal-based nanomaterials can cause an array of adverse cytotoxic effects.[35-38] Therefore, we first focused on prediction of biocompatibility of AuAg-nanorobots in *in Vitro* settings. Cytotoxicity assay with increasing concentrations of fuel and constant concentration of AuAg-nanorobots demonstrated that AuAg-nanorobots are efficiently utilizing hydrogen peroxide as a fuel, which results in protection of cells against its cytotoxic activity. The obtained data show that viability of DU145 cells was significantly higher (Wilcoxon, P = 0.002) in conditions where AuAg-nanorobots were present compared to treatment containing fuel only (**Supplementary Fig. 2A**). Results of cytotoxicity screenings lead us to utilize the fuel concentration threshold of 0.025%, which was the highest fuel concentration used as a

fuel in follow-up experiments. Importantly, hydrogen peroxide is not biocompatible by itself; therefore, it does not present an ideal fuel to be used within biological systems. However, previously published studies have demonstrated that low concentrations of hydrogen peroxide (up to 2.5 wt %) are efficient to induce the movement of nanorobots in biological environment and are tolerated by biological systems.[19, 39-40] In addition, it is worth to note, that our results show that AuAg-nanorobots exhibit a concurrent profound protective function against hydrogen peroxide-induced cytotoxicity (**Supplementary Fig. 2A**) by its decomposition to water and oxygen.[39] It is plausible that hydrogen peroxide-powered nanorobots could be used to treat cancer in parts of the body where hydrogen peroxide cannot cause damage, particularly skin cancer or tumors of the oral cavity.[41] Nevertheless, fully aware of hydrogen peroxide drawbacks, it has to be stated that it is of utmost importance to further research biocompatible sources of power capable to fuel nanorobots used in biological systems, such as a rotating magnetic field or ultrasound.[42-44]. This shall speed up potential *in vivo* application of nanorobots significantly.

It was further revealed that despite their positive charge, AuAg-nanorobots formed only neglectable hard protein corona when being incubated with human plasma, suggesting exceptional stability and inertness of AuAg-nanorobots in blood circulation (**Supplementary Fig. 2B**). This is of utmost importance, since hard protein corona consisting of irreversibly bound blood proteins has an impact on biodistribution of nanoparticles, cellular recognition and uptake, presents a challenge to nanomedicine.[45] Importantly, 2 h exposure of high amount (1×10^{10}) of AuAg-nanorobots to DU145 cells revealed no genotoxic damage that could be expected due to a release of Ag ions from the catalytic shell of AuAg-nanorobots (**Supplementary Fig. 2C**). In overall, array of *in Vitro* analyses confirmed exceptional biocompatibility of AuAg-nanorobots and underpinned their applicability for further experiments. This is in line with the previously published studies demonstrating a high

biocompatibility of Au nanomaterials.[15, 33, 46-48] The obtained results clearly show a potential of synthesized AuAg-nanorobots for use in biomedical research.

The speed of cellular internalization of AuAg-nanorobots markedly increases with exogenous fuel

Au core is a crucial part of AuAg-nanorobots. Au has an excellent biocompatibility causing no immune response and has been widely used for many biological applications aiming for translation to clinics. Similarly, non-viral synthetic vectors such as cationic lipids and polymers have been widely used as well. However, they can be toxic, low efficient in *in Vivo* settings and lack the capability of being easily traced, which is an undisputable advantage of Au.[49-50] Inherent localized surface plasmon resonance of AuAg-nanorobots represents an efficient and unique way for a label-free tracing of motion and bioaccumulation of nanorobots.[51]. Contrary to commonly used organic dyes that exhibit low *in Vivo* stability and can be considerably toxic, Au does not require any further labelling.[52] Considering this, we used surface plasmon resonance as a way of tracing AuAg-nanorobots in all following experiments. First, AuAg-nanorobots were tested for kinetics of their uptake in DU145 prostate cancer cells line in media without fuel (referred to as "static"), to observe non-fueled speed of cellular internalization **(Fig. 1A).** Au-NPs of equal morphology and dimensions were used as a control. First signs of internalization of static AuAg-nanorobots were observed after 4 h incubation, while internalization of Au-NPs could be seen at 12 h time-point, indicating the stimulatory effect of Ag catalytic layer on internalization of nanoparticles possessing the same Au core (**Fig. 1A**).

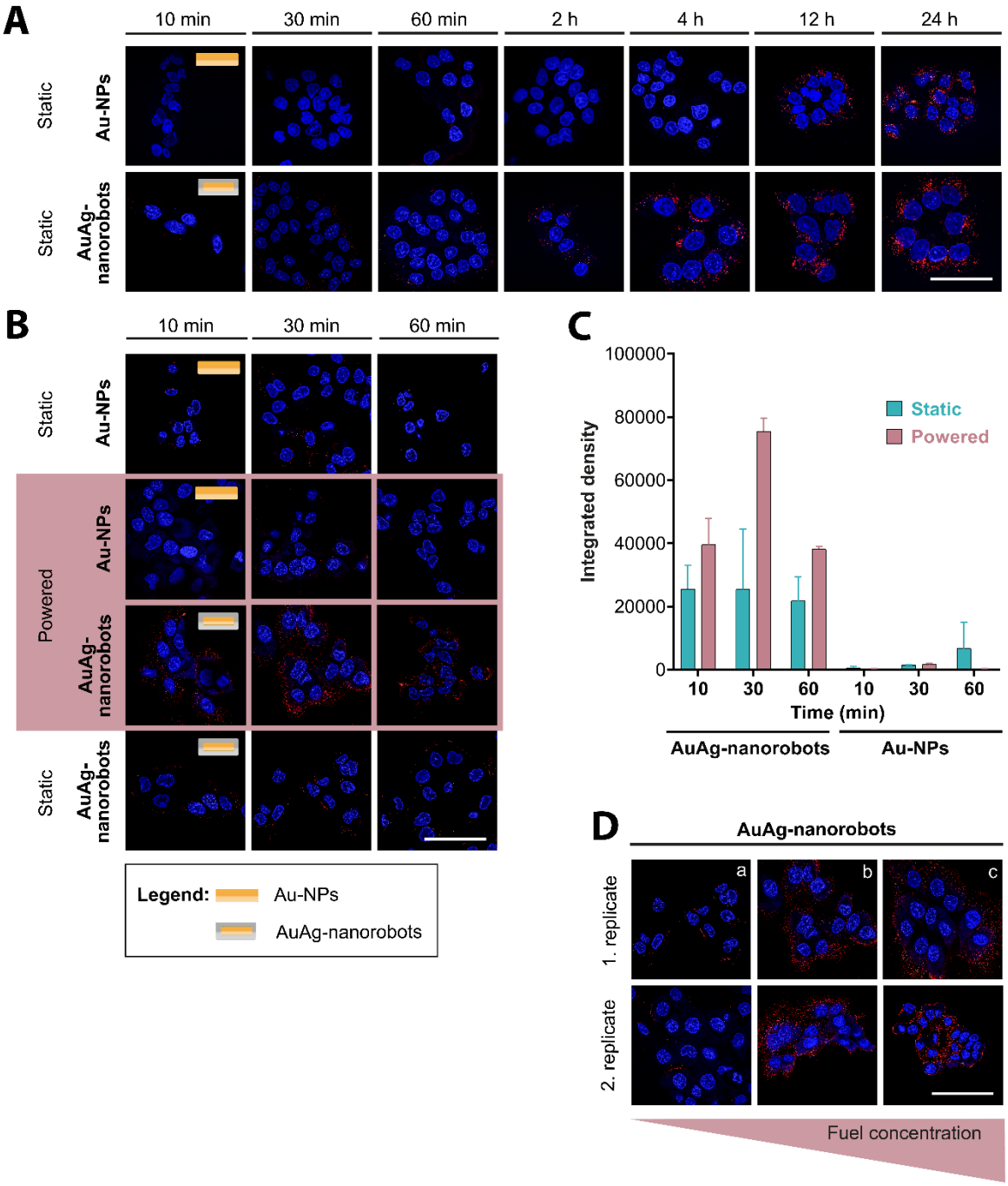

Figure 1: Temporal evaluation of uptake of AuAg-nanorobots. (**A**) AuAg-nanorobots (2×10^7) and size and morphology-relevant Au-NPs (2×10^7) were incubated in fuel-free media to observe the internalization rate into cells without fuel (referred to as "static"). The micrographs show only minor differences in the speed of internalization between static AuAg-nanorobots and Au-NPs. Scale bar, 50 µm. (**B**) Comparative evaluation of cellular internalization of AuAg-nanorobots (2×10^8) and Au-NPs (2×10^8) either in non-fueled

medium (static) or in medium with the addition of 0.0125% fuel (powered). Powered AuAg-nanorobots were internalized already in the 10-min time-point, whereas internalization of static AuAg-nanorobots and AuNPs did not change in this time. Scale bar, 50 μm. (**C**) Integrated density of uptake of powered and static AuAg-nanorobots (2×10^8) and Au-NPs (2×10^8) calculated from replicated confocal reflectance micrographs. Data are presented as mean ± SD. (**D**) The speed of cellular internalization of AuAg-nanorobots is dependent on the concentration of H_2O_2. Images from left to right: (**a**) no fuel, (**b**) 0.0125% fuel, (**c**) 0.025% fuel. AuAg-nanorobots are more densely packed around cells in higher concentrations of fuel, which indicates faster internalization into cells. Note, that the middle micrograph (1. replicate, **b**) was captured under the same experimental conditions as AuAg-nanorobots powered with 0.0125 % fuel after 30 min shown in (**B**) and is therefore the same. Scale bar, 50 μm.

Subsequently, AuAg-nanorobots and Au-NPs (2×10^8) were incubated in fueled (0.0125% fuel) and non-fueled media and internalization was investigated in shorter time-points (10, 30 and 60 min) (**Fig. 1B**). The obtained data revealed notable differences in the speed of internalization into cells between powered and static AuAg-nanorobots. In fuel-containing media, significant cellular internalization could be observed already after 10 min of incubation. In contrast, static AuAg-nanorobots in non-fueled media exhibited no change in the internalization in given time-points and the internalization remained about the same (**Fig. 1B**). Au-NPs lacking Ag catalytic layer did not internalize even after 60 min in spite of using fuel. It is clear that AuAg-nanorobots exhibit enhanced efficiency of cellular internalization after the addition of fuel.

Confocal reflectance microscopy (CRM) micrographs captured in different time-points were used to quantify the integrated density of static and powered AuAg-nanorobots and static and powered Au-NPs shown in **Fig. 1C**. Due to the binarization of CRM micrographs, integrated density corresponds with the area of the image occupied by AuAg-nanorobots. As shown, the

30 min time-point is the peak value for powered AuAg-nanorobots, whereas longer time-points exhibit lower values of integrated density. This is due to the increase of local concentration of AuAg-nanorobots upon entering the cell, thus decreasing the number of pixels, which counts toward the integrated density after thresholding.

Since we showed that powered AuAg-nanorobots massively internalized into cells in just <10 min compared to Au-NPs, which exhibited significantly slower internalization (range of hours), the use of AuAg-nanorobots for dynamic transport of biologically active molecules might be time-saving, and simultaneously increasing the efficiency of such applications.

Further, we wondered whether the concentration of fuel might have an impact on the rate of cellular internalization of AuAg-nanorobots. With this in mind, cells were incubated for 30 min with the same amount of AuAg-nanorobots (2×10^8) in medium containing no fuel (**Fig. 1D-a**), 0.0125% fuel (**Fig. 1D-b**), and 0.025% fuel (**Fig. 1D-c**). As a result, increased concentration of fuel indeed speeded up the cellular internalization and AuAg-nanorobots were tightly packed around cells after 30 min. This demonstrates that the response of AuAg-nanorobots is dose-dependent on the concentration of fuel. However, it is necessary to compromise cell viability with rate of cellular internalization for a desirable effect. Importantly, in all experiments, nuclear counterstaining revealed that application of fuel did not cause deleterious effects on nuclear structures (chromatin condensation and fragmentation commonly used to examine the nuclear damage).[53-54] Thus, our findings indicate a high catalytic efficiency of AuAg-nanorobots resulting in a protection of cells against harmful effects of utilized fuel.

Powered AuAg-nanorobots use caveolin-based endocytic route and are stored in lysosomes

We were further interested whether upon seeming internalization AuAg-nanorobots reside within the cell area and are therefore truly internalized. For this purpose, AuAg-nanorobots (2×10^8) were incubated with DU145 cells in fueled medium (0.025% fuel). As shown in **Fig.**

2A, AuAg-nanorobots were observed within the region of cells demarcated by F-actin cytoskeleton staining, but not in nuclei. This was further validated by construction of the orthogonal projections of Z-stack (**Fig. 2B**). Further, the fate of AuAg-nanorobots in the intracellular space was inspected through Z-stack-based colocalization studies (**Fig. 2C**). Upon 10 min incubation of AuAg-nanorobots (2×10^8) with DU145 cells in fueled media (0.025% fuel), it was found that powered AuAg-nanorobots utilize mainly the caveolin-based internalization route and after 24 h, majority of AuAg-nanorobots colocalize with Lamp-1/2, and are therefore stored in lysosomes (**Fig. 2C**). Quantitation of M1/M2 colocalization coefficients shown in **Fig. 2D** underpins that majority of AuAg-nanorobots is internalized through caveolin-based endocytic route and are subsequently stored in lysosomes. Degree of colocalization with Dynamin, a protein involved in clathrin-dependent endocytosis is low. The caveolin-based internalization route represents a clathrin-independent route, which is an energy-dependent route of uptake, a predominant endocytic route for Au-NPs. After invagination, Au-NPs end up in endosomes, which are eventually fused with lysosomes. This phenomenon is however dependent on the size, shape, charge and surface modification of such nanoparticles.[55-57] The endocytic route ending in lysosomes can by bypassed by various surface modification of Au-NPs such as by using cell penetrating peptides or endosomal disruptive polymers.[58] We anticipate that additional surface engineering of AuAg-nanorobots could result in alteration of prominent endocytic pathway of AuAg-nanorobots towards direct internalization into intracellular region without invagination into endosomes. This will substantially enhance the efficiency of payload transport without its possible inactivation by harsh environment of endolysosomal compartment and without loss of intracellular concentration of payload by lysosomes-mediated exocytosis.

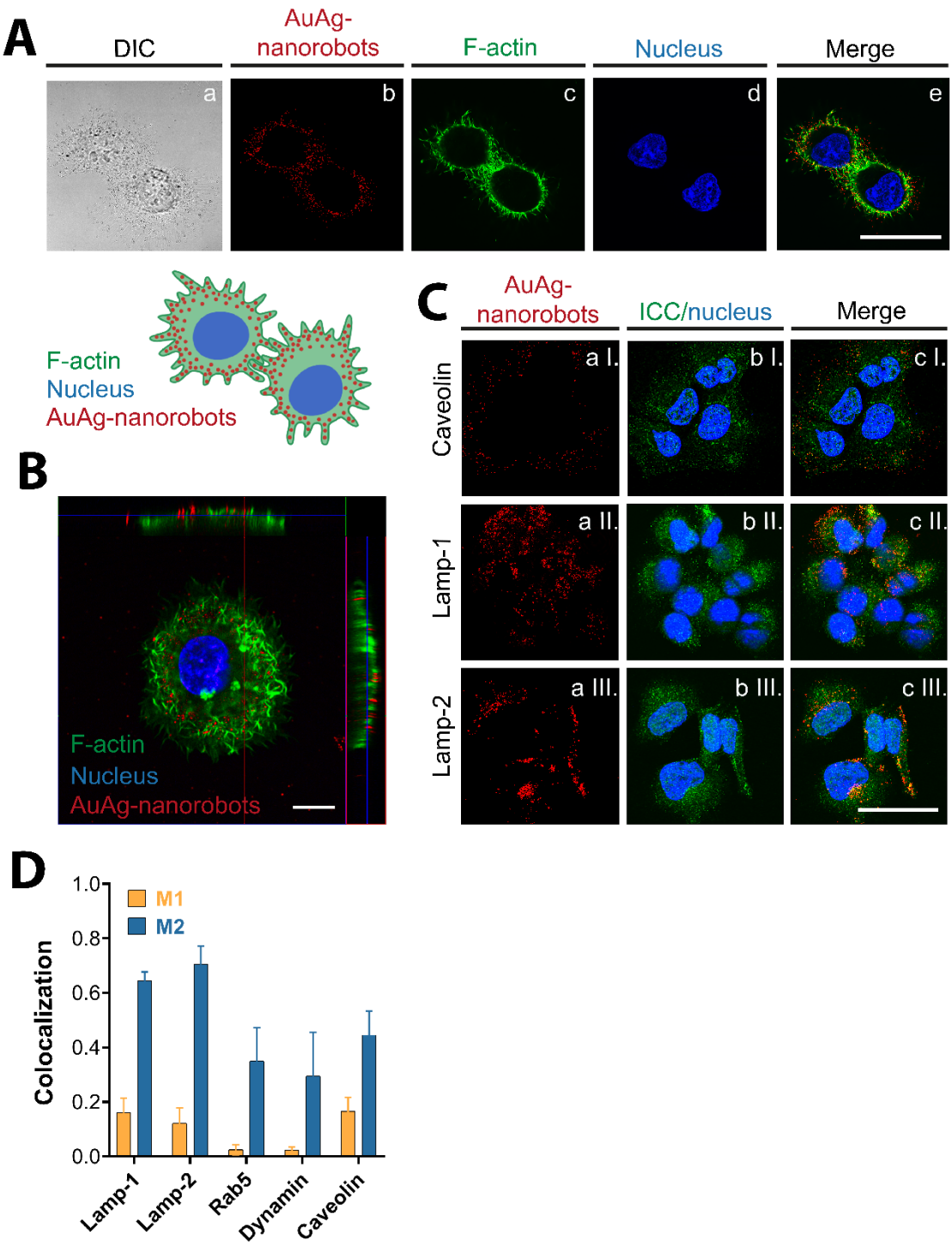

Figure 2: Evaluation of intracellular fate of powered AuAg-nanorobots. (**A**) After 30 min, AuAg-nanorobots reside within the region of cell marked by F-actin staining. (**a**) Represents differential interference contrast (DIC) micrograph of cells, (**b**) represents plasmon resonance signal of AuAg-nanorobots, (**c**) represents fluorescently labeled F-actin cytoskeleton, (**d**)

represents fluorescently labeled nucleus, and (**e**) represents merged image of these micrographs. Scale bar, 100 μm. Drawing mimics merged image. (**B**) Orthogonal projection of Z-stack image of powered AuAg-nanorobots fueled with 0.025% fuel (30 min) shows that AuAg-nanorobots reside within the cell. Scale bar, 10 μm. (**C**) Representative micrographs from colocalization studies of powered AuAg-nanorobots with various immunolabeled endosomal and lysosomal proteins. (**a**) shows plasmon resonance signals of AuAg-nanorobots, (**b**) shows immunocytochemically (ICC)-labeled protein and nucleus, and (**c**) shows merged images. The data show extensive colocalization of powered (0.025% fuel) AuAg-nanorobots with ICC-labeled endocytic marker Caveolin (row I) (after 10 min incubation) and lysosomal markers Lamp-1 and Lamp-2 (rows II and III) at the experimental end-point, 24 h. Scale bar, 100 μm. (**D**) Colocalization analysis of AuAg-nanorobots with ICC-labeled endosomal proteins (Rab-5, Dynamin, Caveolin) and lysosomal proteins (Lamp-1 and Lamp-2) represented by M1 and M2 coefficients. M1 coefficient indicates the degree of overlap of the protein signal with the AuAg-nanorobots channel. M2 coefficient indicates the degree of overlap of the AuAg-nanorobots channel with the protein signal. M2 coefficient indicates that AuAg-nanorobots strongly colocalize with proteins. Data are presented as mean ± SD.

Powered AuAg-nanorobots serve as a dynamic delivery system for metallothionein

As a model protein for the delivery by AuAg-nanorobots, we selected MT, a small, cysteine-rich protein with a capacity to protect cells against toxicity of metal ions and free radicals.[59] Many studies highlighted the role of MT in cancer, which is however not universal and differs in different cancer types.[60] In DU145 cells, MT has been shown to have antiproliferative properties and general tumor suppressive role.[61] Another study highlighted that MT plays a role in growth inhibition of prostate cancer cells.[62] Moreover, downregulation of MT has been

suggested as a biomarker of aggressive prostate cancer in cancer patients.[63] These properties of MT make it an interesting cargo to be delivered using nanomedicines.

To investigate the use AuAg-nanorobots as a powered dynamic delivery system for MT, we first explored whether AuAg-nanorobots can bind fluorescently labeled MT. For this purpose, MT-Cy2 alone and MT-Cy2 bound to AuAg-nanorobots were run on sodium dodecyl sulfate polyacrylamide gel electrophoresis (SDS-PAGE). There was a clear retardation of MT-Cy2 carried by AuAg-nanorobots suggesting efficient binding of Cy2-MT on surface of AuAg-nanorobots (**Fig. 3A**). As shown in **Fig. 3B**, no dramatic shifts in the fluorescence spectrum of Cy2 were detected after MT-Cy2 binding to AuAg-nanorobots, indicating the functionality of Cy2 label and its applicability in further experiments. Furthermore, from spectral analyses it was calculated that loading efficiency of 4 μg of Cy2-labeled MT bound on 2×10^8 of AuAg-nanorobots was ~89%, which equals to ~3.5 μg of Cy2-labeled MT on 2×10^8 of AuAg-nanorobots.

Mammalian MTs contain 20 cysteines with thiol side-chains on which the bioactivity of MTs depends.[64] To test whether MT remains bioactive upon binding to AuAg-nanorobots, we carried out Ellman's colorimetric assay with 5,5′-dithiobis-(2-nitrobenzoic acid) (DTNB), which is based on the cleavage of DTNB by free thiol groups of MT to TNB as described by Shaw *et al*.[65] As shown in **Fig. 3C**, the capability of MT bound to AuAg-nanorobots to cleave DTNB was decreased by ~18.3% compared to free non-bound MT. Such decline is plausibly due to blocking of some thiol moieties caused by their coordination with the surface of AuAg-nanorobots. Noteworthy, the obtained data highlight that the majority of thiol moieties in the MT structure are available, thus the binding of MT to AuAg-nanorobots does not result in overall loss of bioactivity of the protein cargo.

Finally, AuAg-nanorobots (2×10^8) carrying MT-Cy2 were incubated with DU145 cells with and without fuel (0.025% fuel) and imaged in real-time using CRM in 15-sec intervals. Live

cells imaging identified a clear acceleration of cellular internalization of powered AuAg-nanorobots carrying MT-Cy2 (**Fig. 3D**). Micrographs from more time-points are shown in **Supplementary Fig. 3**. MT-Cy2 without AuAg-nanorobots was not able to internalize into cells. Integrated density of AuAg-nanorobots calculated from the obtained micrographs in different time points of live imaging manifested marked difference between powered and static MT-Cy2 carrying AuAg-nanorobots (P =0.004). Powered AuAg-nanorobots were up to 6-fold more efficient in internalization into cells during protein transfection compared to static AuAg-nanorobots (**Fig. 3E**). Colocalization studies performed on micrographs in 10 min time-point revealed a high degree of colocalization of MT-Cy2 with AuAg-nanorobots indicating that majority of MT-Cy2 was carried into cells bound on AuAg-nanorobots (**Fig. 3F**). Our system proved to be useful for a swift protein delivery to hard-to-transfect cancer cell line DU145. It is worth to note that our system is not versatile and every payload will require an extensive optimization of binding conditions and stability under the fueled conditions.

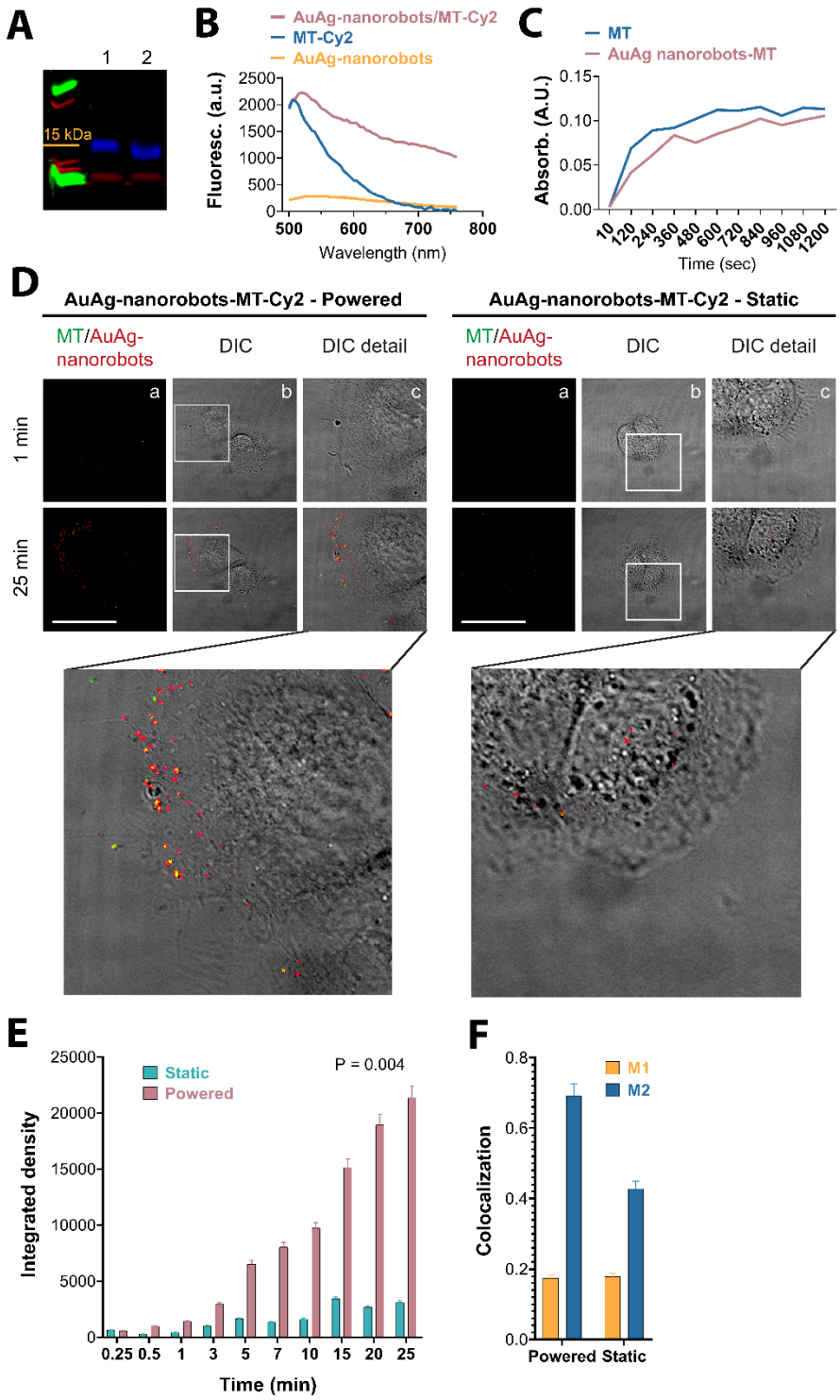

Figure 3: Powered AuAg-nanorobots as a tool for dynamic transfection of protein-based (MT) payload. (**A**) Retardation of Cy2-labeled MT gel migration due to the binding to AuAg-nanorobots. MT was labeled with fluorescent dye Cy2, incubated with AuAg-nanorobots and run on 12% SDS-PAGE to observe retardation due to a binding of MT to AuAg-nanorobots

(lane 1) compared to MT alone (lane 2). (**B**) Fluorescence spectra demonstrating fluorescence properties of Cy2-labeled MT compared to Cy2-labeled MT bound to AuAg-nanorobots. No significant shift in fluorescence spectra indicates unchanged properties of Cy2. (**C**) Colorimetric Ellman's assay representing the bioactivity of MT through accessibility of thiol moieties of free MT and MT bound to AuAg-nanorobots. (**D**) Representative micrographs showing spatiotemporal kinetics of cell uptake of AuAg-nanorobots-MT-Cy2 (2×10^8 of AuAg-nanorobots) in fueled (powered) and non-fueled (static) form. (**a**) represents fluorescence micrographs of MT-Cy2 on AuAg-nanorobots with red being plasmon resonance of AuAg-nanorobots and green being the signal of MT-Cy2, and (**b**) represents DIC micrographs merged with (**a**). **(c**) Represents a zoom of image (**b**). Scale bar, 20 μm. (**E**) Comparative evaluation of integrated density of uptake of static and powered AuAg-nanorobots in annotated time-points using CRM micrographs data from (**D**) and **Supplementary Figure 3**. Powered AuAg-nanorobots internalize more efficiently into cells than static AuAg-nanorobots (Wilcoxon, P = 00.4). Data are presented as mean ± standard error. (**F**) Colocalization analysis of 10 min time-point showing that majority of MT-Cy2 was transfected *via* nanorobots. Colocalization of MT-Cy2 with reflection spots of AuAg-nanorobots. M1 coefficient indicates the degree of overlap of AuAg-nanorobots with Cy2-labeled MT channel. M2 coefficient indicates the degree of overlap of Cy2-labeled MT with AuAg-nanorobots channel. M2 coefficient indicates strong colocalization of Cy2-labeled MT with AuAg-nanorobots. Error bars represent standard error.

Proteins proved an attractive treatment modality of various diseases and market with protein therapeutics has been blooming.[66] Monoclonal antibodies used to treat autoimmune and inflammatory diseases or cancer, among them immune checkpoint inhibitors changing the paradigm of cancer immunotherapy forever,[67-69] proteins that substitute for deficient protein in the treatment of diabetes or hemophilia or protein therapeutics used in the treatment of HIV

or transplant rejection. These are just few clinical applications of protein therapeutics routinely used in clinics. The basic research of protein therapeutics has been as well moving forward with nanomedicine being a strong player in the field of protein therapeutics delivery.[70] In the research race for new treatment modalities there has been also a need for stable transfections of nucleic acids and proteins into cells in order to study protein function in the intracellular space.[71] Viruses proved to be effective delivery tools but the fear of their immunogenicity and oncogenic potential[4-5] is steadily pushing them aside, making space for new technologies coming from fields of nanotechnology and biomaterials.[72] Considering nowadays used transfection agents and their high cytotoxicity in certain cell lines coupled with low transfection efficiency, nanorobots have a great potential to take their place in protein delivery into these cells not only for the interests of basic research. Smart nanorobots hold a strong potential in future translational medical research.

Conclusions

We present chemically powered AuAg-nanorobots capable of enhanced diffusion used for the dynamic transfection of protein-based payload (MT) into DU145 cells known to be difficult-to-transfect by commercially available transfection agents. AuAg-nanorobots as well as amounts of hydrogen peroxide used as the fuel proved to be biocompatible for the purposes of protein transport, generating no cytotoxic and genotoxic damage. The size of AuAg-nanorobots is a great advantage for cell internalization because micron-sized robots are too big to be safely internalized into cells and, therefore, too big to be used in biological applications. The internalization into cells showed to be rapid as AuAg-nanorobots internalized in matter of minutes upon adding of fuel compared to AuAg-nanorobots in non-fueled conditions. We provide the evidence of the use of dynamic nano-scaled delivery systems for fast and rapid intracellular delivery of protein-based payload. Overall, the presented study suggests a potential application of the chemically powered nanorobots not

only for a direct delivery of proteins avoiding common DNA transfection protocols in research laboratories, but also for possible future application in dynamic protein-based therapy of a broad spectrum of diseases. Because protein therapeutics research is now in the limelight, it is desirable to let nanomedicine, and specifically nanorobotics, play a role in the run offering new technologies to the field that would overcome the drawbacks of today's state-of-the-art and showing that nanorobots are indeed in the future of modern translational medicine.

Methods/Experimental

Chemicals

All chemicals were purchased from Sigma-Aldrich (St. Louis, MO, USA) if not stated otherwise. Primary antibodies purchased from Thermo Fisher Scientific (Waltham, MA, USA) were Caveolin 1 Monoclonal Antibody (Z034, cat.: 03-6000), CD107a (Lamp-1) Monoclonal Antibody (eBioH4A3, Cat.: 14-1079-80), Lamp-2 Monoclonal Antibody (H4B4, cat.: MA1-205), Dynamin 2 polyclonal antibody (cat.: PA1-661) and Rab5 polyclonal antibody (cat.: PA3-915). Secondary goat anti-rabbit antibody conjugated with Alexa Fluor 647 (cat.: ab150079) was purchased from Abcam (Cambridge, UK) and goat anti-mouse conjugated with Cruz Fluor 647 (cat.: sc-516244) was bought from Santa Cruz Biotechnology (Dallas, TX, USA).

Synthesis of AuAg-nanorobots

AuAg-nanorobots were prepared in three steps. First, the core Au nanorods (AuNRs) were prepared by a modification of a protocol for AuNRs synthesis in the presence of Ag nitrate.[73] The specific parameters of synthesis were following: the seed solution (5 mL) consisted of 0.1 M hexadecyltrimethylammonium bromide (CTAB) and 0.25 mM $HAuCl_4$. The growth solution (20 mL) consisted of 0.1 M CTAB; 0.25 mM $HAuCl_4$; 0.375 mM ascorbic acid, and 0.067 mM $AgNO_3$. 134 μL of the seed solution was added to the growth solution and

maintained at 25°C. The as-prepared AuNRs were purified by two centrifugation runs at 5,000×*g* for 20 min and redispersed in 10 mM hexadecyltrimethylammonium chloride (CTAC) aqueous solution until the absorbance of the AuNRs at 390 nm was 2.6 (10 mm pathlength). The second step of the AuAg-nanorobots preparation involved overgrowth of the AuNRs cores by Ag shell. The Ag shell overgrowth was achieved according to.[74] Specifically, 8.6 mL of the as prepared AuNRs solution was diluted by 11 mL of 10 mM CTAC, and 160 μL of 0.1 M Ag nitrate was added. The solution was then left to age for 30 min at 23°C. Subsequently, 160 μL of 0.1 M ascorbic acid and 120 μL of 0.1 M NaOH was added into the solution and the temperature was risen to 60°C, which started the shell overgrowth. The solution was then kept at the temperature under mild stirring for 2 h. The formed AuAg-nanorobots solution was then cleaned by two centrifugation runs at 3,500×*g* for 20 min and redispersed in 1 mM CTAC. In the last step, electrostatically bound CTAC stabilization layer was exchanged with covalently bound analog to CTAB, (16-mercaptohexadecyl) trimethylammonium bromide (MTAB) prepared according to [30]. 10 mL of the as-prepared AuAg-nanorobots were concentrated by a centrifugation run at 3500×*g* for 20 min. Then, 2 mg of MTAB and MilliQ water was added to the remaining sediment to the final volume of 0.4 mL. The solution was then sonicated at 40°C for 1 h and left undisturbed overnight. Next day, the solution was sonicated again for 1 h prior to a dilution with MilliQ water to the original volume of 10 mL. Recovered solution containing AuAg-nanorobots was then centrifuged twice at 3,500×*g* for 20 min and redispersed in MilliQ water to remove the remaining CTAC and unbound MTAB.

Physico-chemical characterization of AuAg-nanorobots

The size distribution and morphology of the synthesized AuAg-nanorobots was determined by high-resolution scanning electron microscope (SEM) with high angle dark field (HADF) transmitted electron detector (MAIA3, Tescan, Brno, Czech Republic) using 30 kV

acceleration voltage. The elemental composition of the AuAg bots was analyzed by energy-dispersive X-ray spectroscopy (EDX) using 200 kV transmission electron microscope (JEOL, Tokyo, Japan) equipped with X-Max 80 detector (Oxford Instruments, Abingdon, UK). Optical characterization of the localized surface plasmon modes of the AuAg bots was examined using UV-Vis spectrophotometry in the range of 300 – 1000 nm (Multiscan Sky, Thermo Fisher Scientific, Waltham, MA, USA). To determine the colloidal stability of the AuAg bots ζ-potential was analyzed in 1 mM KCl (Zetasizer Nano ZS, Malvern, Malvern, UK).

Cell culture

Human prostate cancer cell line DU145 was cultured in full RPMI-1640 with 10% fetal bovine serum (FBS) and in 37°C with 5% CO_2. For splitting, cells were disattached by trypsinization. Medium was discarded and cells were washed with phosphate-buffered saline (PBS, pH 7.4). After that, trypsin was added and cells were incubated for 5 min at 37°C. Cells were washed with medium and centrifuged at 400×*g* for 5 min and then, the pellet was resuspended in a new full medium. Prior analyses, cells were counted using Countess II FL Automated Cell Counter (Thermo Fisher Scientific).

MTT colorimetric assay

In order to assess fuel concentration suitable for experiments with AuAg-nanorobots, cytotoxicity assay was performed using of 3-(4,5-dimethylthiazol-2-yl)-2,5 diphenyltetrazolium bromide (MTT). DU145 cells were seeded onto 96 well flat-bottom plate (5,000 cells per well) and cultured for one day in full RMPI-1640 in 37°C and 5% CO_2. After that, the medium was discarded and full medium with fuel was added into wells creating a final concentration of 1.6%, 0.8%, 0.4%, 0.2%, 0.1%, 0.05%, 0.025%, 0.0125%, 0.00625% and 0.003125% hydrogen peroxide. Then, AuAg-nanorobots were added into three rows of wells (1.6×10^7 AuAg-nanorobots per well) that served as technical replicates. Three other

rows were left without adding AuAg-nanorobots. Following 30 min incubation, 10 μL of MTT (5 μg/mL in PBS) was added to each well and incubated for additional 3h. Then, whole volume was discarded, 100 μL of dimethyl sulfoxide (DMSO) was added to each well and absorbance was recorded at 570 nm with Infinite 200 PRO (Tecan, Maennedorf, Switzerland).

Hard-protein corona-forming assay

To determine a formation of hard protein corona on the surface of AuAg-nanorobots, 50 μL of human plasma was mixed with 50 μL of AuAg-nanorobots (5×10^8). As a negative control, the same number of AuAg-nanorobots was added to 50 μL of PBS. Samples were incubated in thermoblock (37°C, 600 rpm, 35 min). Afterwards, samples were centrifuged (15,000×*g*, 15 min) and washed three times with PBS and two times with MilliQ water. 20 μL of MilliQ water and 10 μL of reducing loading buffer was added to samples and run on 12.5% SDS-PAGE. After staining with Coomassie Brilliant Blue, hard protein corona was visualized using Azure c600 (Azure Biosystems, Dublin, CA, USA).

Single-cell gel electrophoresis (SCGE)

To detect potential inherent genotoxicity of AuAg-nanorobots, SCGE was performed. DU145 cells were seeded onto 24 well-plate (50,000 per well) and cultured for one day in full RMPI-1640. Clean microscope slides were frosted with 0.5% agarose and baked in 50°C for 3 h. Then, cells were treated with 1×10^{10} of AuAg-nanorobots in full medium and incubated for 2 h. As a positive control cells were treated with 250 μM, 125 μM and 70 μM fuel. After incubation, cells were trypsinized and pellet was resuspended in 75 μL of low-melting agarose (CLP, San Diego, CA, USA). Suspension was dropped onto frosted microscope slide and covered with a coverslip. Slides were placed in a fridge to harden. Coverslips were then removed and microscope slides were soaked in lysis solution (2.5 M NaCl, 10 mM Tris, 100 mM Na_2EDTA, pH 10 with added 1% Triton X-100 and 10% DMSO) for 2 h. Following incubation, slides were put into electrophoresis chamber, immersed in alkaline electrophoresis

buffer, placed in 4°C for 20 min and electrophoresed (1.25 V/cm, 300 mA) for 30 min. After that, the slides were washed with MilliQ water and stained with ethidium bromide (2 μg/mL). Imaging of SCGE was done with fluorescence microscope EVOS FL Auto Cell Imaging System (Thermo Fisher Scientific). Analysis was carried out by calculating index of damage based on ranking the length of a smear coming from a cell (from 0 to 4) indicating a genotoxic damage.

Evaluation of spatiotemporal internalization kinetics of AuAg-nanorobots

To study kinetics of internalization of AuAg-nanorobots and control Au nanoparticles (Au-NPs) of equal morphology and dimensions into cells, cells were seeded in an 8-well chamber slide and cultured for one day in full RPMI-1640. Cells were treated with AuAg-nanorobots (2×10^8) or Au nanoparticles (2×10^8) in full, fueled (0.025% or 0.0125% hydrogen peroxide) or non-fueled medium and incubated under paraffin cover. To visualize F-actin network, cells were stained with Alexa Fluor 488 Phalloidin (Thermo Fisher Scientific). For this purpose, cells were fixed using 4% formaldehyde for 10 min and subsequently washed three times with PBS. 0.1% Triton X-100 was used for permeabilization. Cells were washed (3×, PBS) and blocking was done using 1% bovine serum albumin (BSA, 30 min). Then, cells were stained with Alexa Fluor 488 Phalloidin (1:200 in 1% BSA in PBS) and incubated for 45 min at room temperature in the dark. Cells were then washed three times with PBS and counterstained using Hoechst 3342 (1:2,000 in PBS) for 4 min. Finally, chambers were mounted using ProLong Diamond Antifade Mountant (Thermo Fisher Scientific) and immediately investigated as described below.

Imaging of AuAg-nanorobots using confocal microscopy

DIC and fluorescence confocal imaging was carried out alongside with visualization of AuAg-nanorobots by CRM using LSM 880 (Carl Zeiss, Jena, Germany). For purpose of CRM, the backscattered light from AuAg-nanorobots was collected within a detection

window (623-633 nm) upon irradiation by a solid-state 633 nm laser. DAPI and Alexa Fluor 488 were excited with the 405 nm and 488 nm lasers and their emissions were recorded at 445-485 nm and 510-560 nm in the fluorescence mode. Alexa Fluor 647 and Cruz Fluor 647 were excited with the 633 nm laser and emission recorded at 638-756 nm. For colocalization studies and visualization of F-actin, Z-stack micrographs were obtained containing 15 focal planes in approx. 2.5 to 4 µm depending on the size of the cell. Orthogonal projection from Z-stack was constructed using Zen Blue software (Carl Zeiss). Quantification of AuAg-nanorobots was carried out using ImageJ (National Institute of Health, Bethesda, MD, USA) by calculating integrated density of AuAg-nanorobots and Au-NPs from replicate micrographs.

Colocalization analyses

For colocalization studies, DU145 cells were seeded in an 8-well chamber slide (30,000 cells per well) and cultured for one day in full RMPI-1640. After that, cells were treated with AuAg-nanorobots (2×10^8) in fueled (0.025% hydrogen peroxide) or non-fueled medium. Chamber slides with cells were covered with parafilm and incubated at 37°C. With respect to the mechanisms of lysosomal biology, before staining of Lamp-1 and Lamp-2, cells were washed three times with phosphate buffered saline (PBS) after 1 h of incubation with AuAg-nanorobots and incubated for another 24 h. In case of staining for endocytosis-related proteins, cells were incubated with AuAg-nanorobots (2×10^8) in fueled (0.025% hydrogen peroxide) or non-fueled medium for 10 min. After washing three times with PBS and fixing with 4% formaldehyde in PBS (15 min), the cells were washed with PBS-T (3×) and permeabilized using 0.25% Triton X-100. After additional washing (3×, PBS), blocking with 5% BSA in PBS (60 min) was carried out. Then, primary antibodies were applied in a dilution specified by the manufacturer diluted in antibody buffer (1 mg/mL BSA in PBS) and cells were incubated over-night at 4°C. On the following day, cells were washed three times with PBS-T

and secondary fluorochrome-conjugated antibody was applied (1:500 in antibody buffer) and cells were incubated for 2 h at room temperature. After three-time PBS-T wash, cells were counterstained using Hoechst 33342 (1:2,000 in PBS for 4 min). Chambers were then mounted using ProLong Diamond Antifade Mountant (Thermo Fisher Scientific). Finally, cells were visualized at CRM (AuAg-nanorobots) and fluorescence (endolysosomal markers) modes using LSM 880 (Carl Zeiss). Z-stack images were analyzed in replicates for quantification of colocalization using ImageJ (National Institute of Health). Mander's coefficients M1 and M2 indicating degree of overlap of two channels were calculated with the use of JACoP plugin.

MT labelling with Cy2 NHS ester dye (Cy2)

MT (metallothionein-1, cell culture grade, Enzo Life Sciences, Farmingdale, NY, USA) was labeled with Cy2 by incubation of 40 µg of MT with 800 pmol of Cy2 in borate buffer (boric acid, sodium tetraborate, pH 8.5) for 1 h on a rotator. Afterwards, mixture was transferred to 3K Amicon Ultracentrifugal Filters and centrifuged (6,000×*g*, 15 min). This process was followed by four washes with borate buffer performed by centrifugation (6,000×*g*, 15 min). Supernatants from all washes and final solution were analyzed for absorption and fluorescence spectra on Infinite 200 PRO (Tecan) to ensure that Cy2 is bound to MT and no residual unbound Cy2 is left in the solution.

Binding of Cy2-MT to AuAg-nanorobots

For the purpose of binding of Cy2-MT onto AuAg-nanorobots, 4 µg of Cy2-MT were incubated with 2×10^8 of AuAg-nanorobots (per sample) in thermoblock (22°C, 450 rpm) for 24 h. Cy2-MT alone was incubated as well and further used as a control. 2 µg Cy2-MT and 2 µg of Cy2-MT bound to AuAg-nanorobots (Cy2-MT-AuA-bots) were loaded on 12.5% SDS-PAGE gel in non-reducing loading buffer to observe retardation of Cy2-MT on AuAg-nanorobots. In addition, Cy2-MT and Cy2-MT-AuA-bots as well as AuAg-nanorobots alone

were analyzed for fluorescence spectra with Infinite 200 PRO (Tecan). Fluorescence spectra were further used to calculate the loading efficiency of MT to AuAg-nanorobots. For the purposes of schematic representation of MT and AuAg-nanorobots binding payload (MT-1A), a 3D structure was constructed from the MT-1A sequence (Uniprot ID 11957) by homology modeling, using the closest homolog crystal structure available as a template (rat MT-2, PDB ID 4MT2). The template sequence had 85.25% identity to the MT-1A with the QMEAN quality score of model −3.76. Molecular structure was calculated after adding hydrogens to the model. Visualization of the structure was done using UCSF Chimera v.1.14.

Ellman's colorimetric assay

To evaluate bioactivity of MT upon binding to AuAg-nanorobots, 2 μg of MT was incubated with 1×10^8 of AuAg-nanorobots (per sample) in a thermoblock (22°C, 450 rpm) for 24 h. After binding, MT and MT bound to AuAg-nanorobots were incubated with 100 μL of 5 mM DTNB solution and immediately analyzed at 412 nm using Infinite 200 PRO (Tecan) in 10 second intervals.

Dynamic delivery of Cy2-MT using AuAg-nanorobots

DU145 cells were seeded on Petri dishes suitable for confocal microscope (175,000 cells per dish) and cultured for one day in full RMPI-1640. Then, cells were treated with Cy2-MT-AuAg-nanorobots dispersed in fueled (0.025% hydrogen peroxide) or non-fueled medium. Cells were visualized by real-time CRM and DIC in living cells imaging mode with 100 cycles of 15 s each. Integrated density of AuAg-nanorobots from acquired images was measured using ImageJ software (National Institute of Health). M1 and M2 colocalization coefficients of Cy2 signal and AuAg-nanorobots in images taken in 10 min time-points were calculated using JACoP plugin in ImageJ software.

Software and statistical analysis

All graphs including statistical analysis were made in GraphPad Prism 8 (GraphPad, San Diego, CA, USA). Images for figures were processed in Adobe Lightroom Classic (Adobe, San Jose, CA, USA). Images were analyzed using ImageJ (National Institute of Health). **Scheme 1** and picture of cells in **Figure 2A** were created with BioRender.com (2020).

Conflict of interests

The authors declare that they have no conflict of interests.

Acknowledgements

V.A. acknowledges funding from the European Research Council (ERC) under the European Union´s Horizon 2020 Research and Innovation Programme (grant agreement No. 759585). V.A. and Z.H. were supported by the Czech Science Foundation (project no. 19-13766J). M.P. was supported by Ministry of Education, Youth and Sports (Czech Republic) grant LL2002 under ERC CZ program. M.P. was supported by Ministry of Education, Youth and Sports (Czech Republic) grant LL2002 under ERC CZ program.

Authors' contributions

Z.H. and M.P. conceptualized the study. A.R. performed experiments with cell cultures, optimized labelling of MT and its binding to AuAg-nanorobots and performed image analyses, F.N. synthetized nanoparticles and performed their physico-chemical characterization, H.M. performed imaging using CRM and fluorescence microscopy, M.P. supervised AuAg-nanorobots fabrication and discussed overall results, V.A. supervised analytical part of the experiment and discussed the overall results, Z.H. designed and supervised biological experiments and experiments using CRM. All authors participated on manuscript preparation and agree with its final form.

Supporting Information

The Supporting Information is available free of charge online at http://pubs.acs.org.

- Physico-chemical characterization of the AuAg-nanorobots (PDF)
- Cytotoxicity screening to assess biocompatiblity of AuAg-nanorobots (PDF)
- Representative micrographs showing spatiotemporal kinetics of uptake of AuAg-nanorobots-MT-Cy2 (PDF)

References

(1). Wells, D. J. Gene Therapy Progress and Prospects: Electroporation and Other Physical Methods. *Gene Ther.* **2004,** *11*, 1363-1369.

(2). Bulcha, J. T.; Wang, Y.; Ma, H.; Tai, P. W. L.; Gao, G. Viral Vector Platforms within the Gene Therapy Landscape. *Signal Transduct. Targeted Ther.* **2021,** *6*, 1-24.

(3). Kay, M. A.; Glorioso, J. C.; Naldini, L. Viral Vectors for Gene Therapy: The Art of Turning Infectious Agents into Vehicles of Therapeutics. *Nat. Med.* **2001,** *7*, 33-40.

(4). Cattoglio, C.; Facchini, G.; Sartori, D.; Antonelli, A.; Miccio, A.; Cassani, B.; Schmidt, M.; Von Kalle, C.; Howe, S.; Thrasher, A. J. Hot Spots of Retroviral Integration in Human Cd34+ Hematopoietic Cells. *Blood* **2007,** *110*, 1770-1778.

(5). Colella, P.; Ronzitti, G.; Mingozzi, F. Emerging Issues in Aav-Mediated in Vivo Gene Therapy. *Molecular Therapy-Methods & Clinical Development* **2018,** *8*, 87-104.

(6). Shi, J.; Kantoff, P. W.; Wooster, R.; Farokhzad, O. C. Cancer Nanomedicine: Progress, Challenges and Opportunities. *Nat. Rev. Cancer* **2017,** *17*, 20-37.

(7). Rosenblum, D.; Joshi, N.; Tao, W.; Karp, J. M.; Peer, D. Progress and Challenges Towards Targeted Delivery of Cancer Therapeutics. *Nat. Commun.* **2018,** *9*, 1-12.

(8). Mitchell, M. J.; Billingsley, M. M.; Haley, R. M.; Wechsler, M. E.; Peppas, N. A.; Langer, R. S. Engineering Precision Nanoparticles for Drug Delivery. *Nat. Rev. Drug Discov.* **2021,** *20*, 101-124.

(9). Zhang, L.; Gu, F. X.; Chan, J. M.; Wang, A. Z.; Langer, R. S.; Farokhzad, O. C. Nanoparticles in Medicine: Therapeutic Applications and Developments. *Clinical pharmacology and therapeutics* **2008,** *83*, 761-769.

(10). Moghimi, S. M.; Hunter, C. A.; Murray, C. J. Nanomedicine: Current Status and Future Prospects. *FASEB J.* **2005,** *19*, 311-330.

(11). Ding, Y.; Jiang, Z.; Saha, K.; Kim, C. S.; Kim, S. T.; Landis, R. F.; Rotello, V. M. Gold Nanoparticles for Nucleic Acid Delivery. *Mol. Ther.* **2014,** *22*, 1075-1083.

(12). Sandhu, K. K.; McIntosh, C. M.; Simard, J. M.; Smith, S. W.; Rotello, V. M. Gold Nanoparticle-Mediated Transfection of Mammalian Cells. *Bioconjug. Chem.* **2002,** *13*, 3-6.

(13). Liz-Marzan, L. M. Tailoring Surface Plasmons through the Morphology and Assembly of Metal Nanoparticles. *Langmuir* **2006,** *22*, 32-41.

(14). Elahi, N.; Kamali, M.; Baghersad, M. H. Recent Biomedical Applications of Gold Nanoparticles: A Review. *Talanta* **2018,** *184*, 537-556.

(15). Connor, E. E.; Mwamuka, J.; Gole, A.; Murphy, C. J.; Wyatt, M. D. Gold Nanoparticles Are Taken up by Human Cells but Do Not Cause Acute Cytotoxicity. *Small (Weinheim an der Bergstrasse, Germany)* **2005,** *1*, 325-7.

(16). Boisselier, E.; Astruc, D. Gold Nanoparticles in Nanomedicine: Preparations, Imaging, Diagnostics, Therapies and Toxicity. *Chemical Society reviews* **2009,** *38*, 1759-1782.

(17). Li, J. L.; Wang, L.; Liu, X.-Y.; Zhang, Z.-P.; Guo, H. C.; Liu, W. M.; Tang, S. H. *In Vitro* Cancer Cell Imaging and Therapy Using Transferrin-Conjugated Gold Nanoparticles. *Cancer Lett.* **2009,** *274*, 319-326.

(18). Lee, K.; Conboy, M.; Park, H. M.; Jiang, F.; Kim, H. J.; Dewitt, M. A.; Mackley, V. A.; Chang, K.; Rao, A.; Skinner, C.; Shobha, T.; Mehdipour, M.; Liu, H.; Huang, W.-C.; Lan, F.; Bray, N. L.; Li, S.; Corn, J. E.; Kataoka, K.; Doudna, J. A.; Conboy, I.; Murthy, N. Nanoparticle Delivery of Cas9 Ribonucleoprotein and Donor DNA *in Vivo* Induces Homology-Directed DNA Repair. *Nat Biomed Eng* **2017,** *1*, 889-901.

(19). Villa, K.; Krejcova, L.; Novotny, F.; Heger, Z.; Sofer, Z.; Pumera, M. Cooperative Multifunctional Self-Propelled Paramagnetic Microrobots with Chemical Handles for Cell Manipulation and Drug Delivery. *Adv. Funct. Mater.* **2018,** *28*, 1-8.

(20). Patino, T.; Arque, X.; Mestre, R.; Palacios, L.; Sanchez, S. Fundamental Aspects of Enzyme-Powered Micro- and Nanoswimmers. *Acc. Chem. Res.* **2018,** *51*, 2662-2671.

(21). Yuan, K.; Bujalance-Fernandez, J.; Jurado-Sanchez, B.; Escarpa, A. Light-Driven Nanomotors and Micromotors: Envisioning New Analytical Possibilities for Bio-Sensing. *Microchim. Acta* **2020,** *187*, 1-16.

(22). Chen, X.-Z.; Hoop, M.; Mushtaq, F.; Siringil, E.; Hu, C.; Nelson, B. J.; Pane, S. Recent Developments in Magnetically Driven Micro- and Nanorobots. *Appl. Mater. Today* **2017,** *9*, 37-48.

(23). Yu, J.; Jin, D.; Chan, K.-F.; Wang, Q.; Yuan, K.; Zhang, L. Active Generation and Magnetic Actuation of Microrobotic Swarms in Bio-Fluids. *Nature Commun.* **2019,** *10*, 1-12.

(24). Wang, J., *Nanomachines: Fundamentals and Applications*. John Wiley & Sons, Ltd: **2013**; Vol. 53, p 200.

(25). Venugopalan, P. L.; de Avila, B. E. F.; Pal, M.; Ghosh, A.; Wang, J. Fantastic Voyage of Nanomotors into the Cell. *ACS Nano* **2020,** *14*, 9423-9439.

(26). Novotný, F.; Wang, H.; Pumera, M. Nanorobots: Machines Squeezed between Molecular Motors and Micromotors. *Chem* **2020,** *6*, 867-884.

(27). Wilhelm, S.; Tavares, A. J.; Dai, Q.; Ohta, S.; Audet, J.; Dvorak, H. F.; Chan, W. C. Analysis of Nanoparticle Delivery to Tumours. *Nature reviews materials* **2016,** *1*, 16014.

(28). Gao, W.; Wang, J. Synthetic Micro/Nanomotors in Drug Delivery. *Nanoscale* **2014,** *6*, 10486-10494.

(29). Soto, F.; Chrostowski, R. Frontiers of Medical Micro/Nanorobotics: In Vivo Applications and Commercialization Perspectives toward Clinical Uses. *Front Bioeng Biotechnol* **2018,** *6*, 1-12.

(30). Novotny, F.; Plutnar, J.; Pumera, M. Plasmonic Self-Propelled Nanomotors for Explosives Detection *Via* Solution-Based Surface Enhanced Raman Scattering. *Adv. Funct. Mater.* **2019,** *29*, 1-7.

(31). Wang, H.; Pumera, M. Micro/Nanomachines and Living Biosystems: From Simple Interactions to Microcyborgs. *Adv. Funct. Mater.* **2018,** *28*, 1-17.

(32). Gao, W.; de Ávila, B. E.; Zhang, L.; Wang, J. Targeting and Isolation of Cancer Cells Using Micro/Nanomotors. *Adv Drug Deliv Rev* **2018,** *125*, 94-101.

(33). Zarska, M.; Sramek, M.; Novotny, F.; Havel, F.; Babelova, A.; Mrazkova, B.; Benada, O.; Reinis, M.; Stepanek, I.; Musilek, K.; Bartek, J.; Ursinyova, M.; Novak, O.; Dzijak, R.; Kuca, K.; Proska, J.; Hodny, Z. Biological Safety and Tissue Distribution of (16-Mercaptohexadecyl)Trimethylammonium Bromide-Modified Cationic Gold Nanorods. *Biomaterials* **2018,** *154*, 275-290.

(34). Tebbe, M.; Kuttner, C.; Mayer, M.; Maennel, M.; Pazos-Perez, N.; Konig, T. A. F.; Fery, A. Silver-Overgrowth-Induced Changes in Intrinsic Optical Properties of Gold Nanorods: From Noninvasive Monitoring of Growth Kinetics to Tailoring Internal Mirror Charges. *J. Phys. Chem. C* **2015,** *119*, 9513-9523.

(35). Yang, J.; Luo, M.; Tan, Z.; Dai, M.; Xie, M.; Lin, J.; Hua, H.; Ma, Q.; Zhao, J.; Liu, A. Oral Administration of Nano-Titanium Dioxide Particle Disrupts Hepatic Metabolic Functions in a Mouse Model. *Environ. Toxicol. Pharmacol.* **2017,** *49*, 112-118.

(36). Radziun, E.; Dudkiewicz Wilczyńska, J.; Książek, I.; Nowak, K.; Anuszewska, E. L.; Kunicki, A.; Olszyna, A.; Ząbkowski, T. Assessment of the Cytotoxicity of Aluminium Oxide

Nanoparticles on Selected Mammalian Cells. *Toxicology in Vitro : an international journal published in association with BIBRA* **2011,** *25*, 1694-1700.

(37). Lei, R.; Wu, C.; Yang, B.; Ma, H.; Shi, C.; Wang, Q.; Wang, Q.; Yuan, Y.; Liao, M. Integrated Metabolomic Analysis of the Nano-Sized Copper Particle-Induced Hepatotoxicity and Nephrotoxicity in Rats: A Rapid *in Vivo* Screening Method for Nanotoxicity. *Toxicology and applied pharmacology* **2008,** *232*, 292-301.

(38). Guan, R.; Kang, T.; Lu, F.; Zhang, Z.; Shen, H.; Liu, M. Cytotoxicity, Oxidative Stress, and Genotoxicity in Human Hepatocyte and Embryonic Kidney Cells Exposed to Zno Nanoparticles. *Nanoscale research letters* **2012,** *7*, 1-7.

(39). Wu, Z.; Wu, Y.; He, W.; Lin, X.; Sun, J.; He, Q. Self-Propelled Polymer-Based Multilayer Nanorockets for Transportation and Drug Release. *Angew. Chem. Int. Ed.* **2013,** *52*, 7000-7003.

(40). Khezri, B.; Beladi Mousavi, S. M.; Krejcova, L.; Heger, Z.; Sofer, Z.; Pumera, M. Ultrafast Electrochemical Trigger Drug Delivery Mechanism for Nanographene Micromachines. *Adv. Funct. Mater.* **2019,** *29*, 1-10.

(41). Villa, K.; Viktorova, J.; Plutnar, J.; Ruml, T.; Hoang, L.; Pumera, M. Chemical Microrobots as Self-Propelled Microbrushes against Dental Biofilm. *Cell Reports Physical Science* **2020,** *1*, 100181.

(42). Zhou, H.; Mayorga-Martinez, C. C.; Pané, S.; Zhang, L.; Pumera, M. Magnetically Driven Micro and Nanorobots. *Chemical reviews* **2021**.

(43). Vyskočil, J.; Mayorga-Martinez, C. C.; Jablonská, E.; Novotný, F.; Ruml, T.; Pumera, M. Cancer Cells Microsurgery Via Asymmetric Bent Surface Au/Ag/Ni Microrobotic Scalpels through a Transversal Rotating Magnetic Field. *ACS Nano* **2020,** *14*, 8247-8256.

(44). Garcia-Gradilla, V.; Orozco, J.; Sattayasamitsathit, S.; Soto, F.; Kuralay, F.; Pourazary, A.; Katzenberg, A.; Gao, W.; Shen, Y.; Wang, J. Functionalized Ultrasound-Propelled Magnetically Guided Nanomotors: Toward Practical Biomedical Applications. *ACS Nano* **2013,** *7*, 9232-40.

(45). Charbgoo, F.; Nejabat, M.; Abnous, K.; Soltani, F.; Taghdisi, S. M.; Alibolandi, M.; W., T. S.; Steele, T. W. J.; Ramezani, M. Gold Nanoparticle Should Understand Protein Corona for Being a Clinical Nanomaterial. *J. Control. Release* **2018,** *272*, 39-53.

(46). Shukla, R.; Bansal, V.; Chaudhary, M.; Basu, A.; Bhonde, R. R.; Sastry, M. Biocompatibility of Gold Nanoparticles and Their Endocytotic Fate inside the Cellular Compartment: A Microscopic Overview. *Langmuir* **2005,** *21*, 10644-10654.

(47). Liu, J.; Yu, M.; Zhou, C.; Yang, S.; Ning, X.; Zheng, J. Passive Tumor Targeting of Renal-Clearable Luminescent Gold Nanoparticles: Long Tumor Retention and Fast Normal Tissue Clearance. *J. Am. Chem. Soc.* **2013,** *135*, 4978-4981.

(48). Zheng, K.; Setyawati, M. l. I.; Leong, D. T.; Xie, J. Antimicrobial Gold Nanoclusters. *ACS Nano* **2017,** *11*, 6904-6910.

(49). Godbey, W. T.; Wu, K. K.; Mikos, A. G. Poly(Ethylenimine) and Its Role in Gene Delivery. *J. Control. Release* **1999,** *60*, 149-160.

(50). Lv, H.; Zhang, S.; Wang, B.; Cui, S.; Yan, J. Toxicity of Cationic Lipids and Cationic Polymers in Gene Delivery. *J. Control. Release* **2006,** *114*, 100-109.

(51). Zarska, M.; Novotny, F.; Havel, F.; Sramek, M.; Babelova, A.; Benada, O.; Novotny, M.; Saran, H.; Kuca, K.; Musilek, K.; Hvezdova, Z.; Dzijak, R.; Vancurova, M.; Krejcikova, K.; Gabajova, B.; Hanzlikova, H.; Kyjacova, L.; Bartek, J.; Proska, J.; Hodny, Z. Two-Step Mechanism of Cellular Uptake of Cationic Gold Nanoparticles Modified by (16-Mercaptohexadecyl)Trimethylammonium Bromide. *Bioconjugate Chemistry* **2016,** *27*, 2558-2574.

(52). Alford, R.; Simpson, H. M.; Duberman, J.; Hill, G. C.; Ogawa, M.; Regino, C.; Kobayashi, H.; Choyke, P. L. Toxicity of Organic Fluorophores Used in Molecular Imaging: Literature Review. *Mol. Imaging* **2009,** *8*, 1-14.

(53). Crowley, L. C.; Marfell, B. J.; Waterhouse, N. J. Analyzing Cell Death by Nuclear Staining with Hoechst 33342. *Cold Spring Harb. Protoc.* **2016,** *2016*, 778-781.

(54). Mandelkow, R.; Gümbel, D.; Ahrend, H.; Kaul, A.; Zimmermann, U.; Burchardt, M.; Stope, M. B. Detection and Quantification of Nuclear Morphology Changes in Apoptotic Cells by Fluorescence Microscopy and Subsequent Analysis of Visualized Fluorescent Signals. *Anticancer Res.* **2017,** *37*, 2239-2244.

(55). Chithrani, D. B. Intracellular Uptake, Transport, and Processing of Gold Nanostructures. *Mol. Membr. Biol.* **2010,** *27*, 299-311.

(56). Albanese, A.; Tang, P. S.; Chan, W. C. W. The Effect of Nanoparticle Size, Shape, and Surface Chemistry on Biological Systems. *Annu. Rev. Biomed. Eng.* **2012,** *14*, 1-16.

(57). Tang, H.; Zhang, H.; Ye, H.; Zheng, Y. Receptor-Mediated Endocytosis of Nanoparticles: Roles of Shapes, Orientations, and Rotations of Nanoparticles. *J. Phys. Chem. B* **2018,** *122*, 171-180.

(58). Nativo, P.; Prior, I. A.; Brust, M. Uptake and Intracellular Fate of Surface-Modified Gold Nanoparticles. *ACS Nano* **2008,** *2*, 1639-44.

(59). Coyle, P.; Philcox, J. C.; Carey, L. C.; Rofe, A. M. Metallothionein: The Multipurpose Protein. *Cellular and molecular life sciences : CMLS* **2002,** *59*, 627-647.

(60). Si, M.; Lang, J. The Roles of Metallothioneins in Carcinogenesis. *J Hematol Oncol* **2018,** *11*, 1-20.

(61). Han, Y.-C.; Zheng, Z.-L.; Zuo, Z.-H.; Yu, Y. P.; Chen, R.; Tseng, G. C.; Nelson, J. B.; Luo, J.-H. Metallothionein 1 H Tumour Suppressor Activity in Prostate Cancer Is Mediated by Euchromatin Methyltransferase 1. *The Journal of pathology* **2013,** *230*, 184-193.

(62). Dutta, R.; Sens, D. A.; Somji, S.; Sens, M. A.; Garrett, S. H. Metallothionein Isoform 3 Expression Inhibits Cell Growth and Increases Drug Resistance of Pc-3 Prostate Cancer Cells. *The Prostate* **2002,** *52*, 89-97.

(63). Demidenko, R.; Daniunaite, K.; Bakavicius, A.; Sabaliauskaite, R.; Skeberdyte, A.; Petroska, D.; Laurinavicius, A.; Jankevicius, F.; Lazutka, J. R.; Jarmalaite, S. Decreased Expression of Mt1e Is a Potential Biomarker of Prostate Cancer Progression. *Oncotarget* **2017,** *8*, 61709-61718.

(64). Theocharis, S. E.; Margeli, A. P.; Koutselinis, A. Metallothionein: A Multifunctional Protein from Toxicity to Cancer. *The International journal of biological markers* **2003,** *18*, 162-9.

(65). Shaw, C. F., 3rd; Savas, M. M.; Petering, D. H. Ligand Substitution and Sulfhydryl Reactivity of Metallothionein. *Methods in enzymology* **1991,** *205*, 401-14.

(66). Leader, B.; Baca, Q. J.; Golan, D. E. Protein Therapeutics: A Summary and Pharmacological Classification. *Nat. Rev. Drug Discov.* **2008,** *7*, 21-39.

(67). Robert, C.; Soria, J. C.; Eggermont, A. M. Drug of the Year: Programmed Death-1 Receptor/Programmed Death-1 Ligand-1 Receptor Monoclonal Antibodies. *European journal of cancer (Oxford, England : 1990)* **2013,** *49*, 2968-2971.

(68). Eggermont, A. M. M.; Robert, C. New Drugs in Melanoma: It's a Whole New World. *European journal of cancer (Oxford, England : 1990)* **2011,** *47*, 2150-2157.

(69). Leavy, O. Therapeutic Antibodies: Past, Present and Future. *Nature reviews. Immunology* **2010,** *10*, 297-297.

(70). Yu, M.; Wu, J.; Shi, J.; Farokhzad, O. C. Nanotechnology for Protein Delivery: Overview and Perspectives. *J. Control. Release* **2016,** *240*, 24-37.

(71). Chen, S.-H.; Chao, A.; Tsai, C.-L.; Sue, S.-C.; Lin, C.-Y.; Lee, Y.-Z.; Hung, Y.-L.; Chao, A.-S.; Cheng, A.-J.; Wang, H.-S.; Wang, T.-H. Utilization of Hepes for Enhancing Protein Transfection into Mammalian Cells. *Mol. Ther. Methods Clin. Dev.* **2019,** *13*, 99-111.

(72). Lee, K.; Conboy, M.; Park, H. M.; Jiang, F.; Kim, H. J.; Dewitt, M. A.; Mackley, V. A.; Chang, K.; Rao, A.; Skinner, C. Nanoparticle Delivery of Cas9 Ribonucleoprotein and Donor DNA in Vivo Induces Homology-Directed DNA Repair. *Nature biomedical engineering* **2017,** *1*, 889.

(73). Nikoobakht, B.; El-Sayed, M. A. Preparation and Growth Mechanism of Gold Nanorods (Nrs) Using Seed-Mediated Growth Method. *Chemistry of Materials* **2003,** *15*, 1957-1962.

(74). Park, K.; Drummy, L. F.; Vaia, R. A. Ag Shell Morphology on Au Nanorod Core: Role of Ag Precursor Complex. *J. Mater. Chem.* **2011,** *21*, 15608-15618.

For table of contents only: